Mechanism of Shiga Toxin Clustering on Membranes

Pezeshkian, Weria; Gao, Haifei; Arumugam, Senthil; Becken, Ulrike; Bassereau, Patricia; Florent, Jean Claude; Ipsen, John Hjort; Johannes, Ludger; Shillcock, Julian C.

Published in:
ACS Nano

DOI:
10.1021/acsnano.6b05706

Publication date:
2017

Document version
Publisher's PDF, also known as Version of record

Citation for pulished version (APA):
Pezeshkian, W., Gao, H., Arumugam, S., Becken, U., Bassereau, P., Florent, J. C., ... Shillcock, J. C. (2017). Mechanism of Shiga Toxin Clustering on Membranes. ACS Nano, 11(1), 314-324. DOI: 10.1021/acsnano.6b05706

ACS NANO

www.acsnano.org

ARTICLE

Mechanism of Shiga Toxin Clustering on Membranes

Weria Pezeshkian,[†,#,°] Haifei Gao,[‡,#,°] Senthil Arumugam,[‡,§,°] Ulrike Becken,[‡] Patricia Bassereau,[§,∥] Jean-Claude Florent,[‡] John Hjort Ipsen,[*,†] Ludger Johannes,[*,‡] and Julian C. Shillcock[*,⊥]

[†]Center for Biomembrane Physics (MEMPHYS), Department of Physics, Chemistry and Pharmacy (FKF), University of Southern Denmark, Campusvej 55, 5230 Odense M, Denmark

[‡]Institut Curie, PSL Research University, Chemical Biology of Membranes and Therapeutic Delivery unit, INSERM U 1143, CNRS UMR 3666, 26 rue d'Ulm, 75248 Cedex 05 Paris, France

[§]Laboratoire Physico Chimie Curie, Institut Curie, PSL Research University, CNRS UMR16855216, 75248 Cedex 05 Paris, France

[∥]Sorbonne Universités, UPMC Univ Paris 06, 75005 Paris, France

[⊥]Ecole polytechnique fédérale de Lausanne (EPFL), 1015 Lausanne, Switzerland

[#]TRANSPOL Molecular Neurobiochemistry, Ruhr Universität Bochum, 44801 Bochum, Germany

Supporting Information

ABSTRACT: **The bacterial Shiga toxin interacts with its cellular receptor, the glycosphingolipid globotriaosylceramide (Gb3 or CD77), as a first step to entering target cells. Previous studies have shown that toxin molecules cluster on the plasma membrane, despite the apparent lack of direct interactions between them. The precise mechanism by which this clustering occurs remains poorly defined. Here, we used vesicle and cell systems and computer simulations to show that line tension due to curvature, height, or compositional mismatch, and lipid or solvent depletion cannot drive the clustering of Shiga toxin molecules. By contrast, in coarse-grained computer simulations, a correlation was found between clustering and toxin nanoparticle-driven suppression of membrane fluctuations, and experimentally we observed that clustering required the toxin molecules to be tightly bound to the membrane surface. The most likely interpretation of these findings is that a membrane fluctuation-induced force generates an effective attraction between toxin molecules. Such force would be of similar strength to the electrostatic force at separations around 1 nm, remain strong at distances up to the size of toxin molecules (several nanometers), and persist even beyond. This force is predicted to operate between manufactured nanoparticles providing they are sufficiently rigid and tightly bound to the plasma membrane, thereby suggesting a route for the targeting of nanoparticles to cells for biomedical applications.**

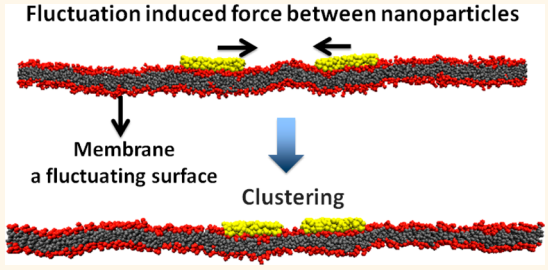

KEYWORDS: *Casimir force, fluctuation-induced force, endocytosis, invagination, membrane, clustering, glycosphingolipid, lectin*

The bacterial Shiga-like toxins from *Escherichia coli* are responsible for pathological manifestations that can lead to hemolytic uremic syndrome, an endemic threat to human health.[1] These toxins are composed of 2 subunits: a catalytic A-subunit, which modifies rRNA once translocated to the cytosol of target cells, leading to protein biosynthesis inhibition;[2] and a homopentameric B-subunit, which mediates the toxin's interaction with glycosphingolipids (GSLs) from the globoseries, which function as cellular toxin receptors.

The cell biology of the parental Shiga toxin from *Shigella dysenteriae* has been particularly well-studied.[2,3] Its B-subunit (STxB), a rigid protein of around 7 nm in diameter, tightly binds up to 15 globotriaosylceramide (Gb3) GSL receptor molecules as the first step leading to toxin entry into cells.[2] Current understanding suggests that the Shiga toxin-driven reorganization of membrane lipids endows the toxin−Gb3 complexes with curvature active properties that after clustering of toxin molecules enables the formation of endocytic membrane invaginations without a strict requirement for the cytosolic clathrin machinery (for a review, see Johannes et al.[4]). After endocytosis, Shiga toxin is then transported from early endosomes to the Golgi apparatus and the endoplasmic reticulum, from where the catalytic A-subunit is translocated to the cytosol to modify rRNA and thereby to inhibit protein biosynthesis.[5]

Received: August 24, 2016
Accepted: December 12, 2016
Published: December 12, 2016

DOI: 10.1021/acsnano.6b05706
ACS Nano 2017, 11, 314−324

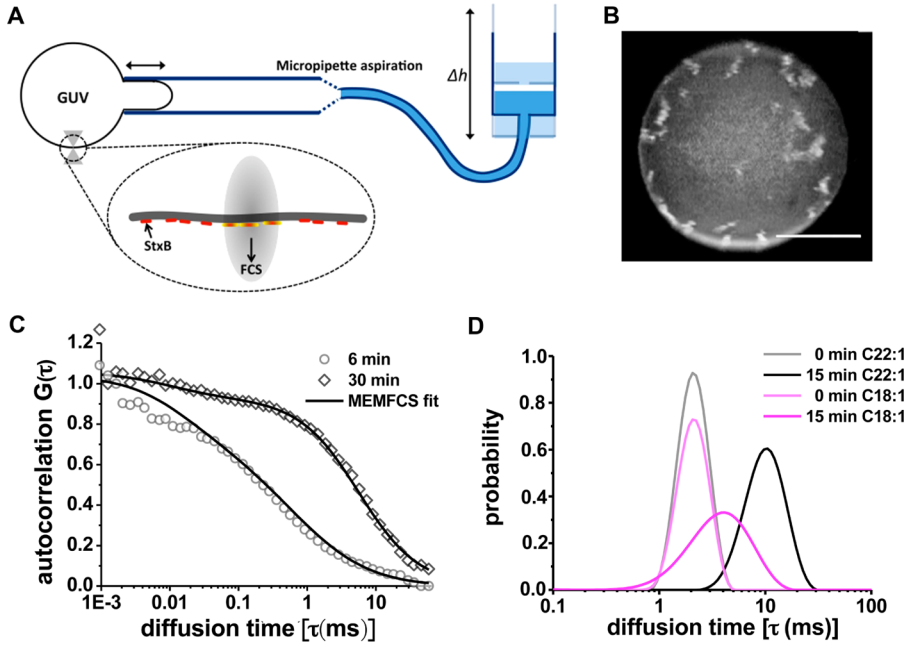

Figure 1. STxB clustering on GUVs. (A) Schematic of the micropipette aspiration system coupled with FCS. (B) GUV composed of 30% Gb3 and 70% DOPC under low membrane tension displays STxB clustering and tubulation. Scale bar 10 μm. (C) Normalized autocorrelation curves of 200 nM STxB-Alexa488 on GUVs tensed using micropipette aspiration at different time points. The continuous line is the MEMFCS fit of the data. (D) Distributions of τ_D obtained from MEMFCS fitting of STxB clustering on vesicles prepared with 5 mol % C22:1 (black and gray traces) or C18:1 Gb3 (pink traces) and DOPC (95 mol %) at different time points. STxB clusters in interaction with both lipid species.

Shiga toxin forms clusters on cell and model membranes despite the apparent absence of direct protein−protein interaction between toxin molecules based on hydrophobic or electrostatic effects, or mechanisms based on cholesterol-dependent phase separation.[6] How this clustering occurs is still unknown. Possible mechanisms for membrane-associated particle clustering are based on acto-myosin-driven molecular focusing, which would operate at length scales in the range of tens to hundreds of nanometers,[7,8] and membrane-mediated forces in which the particles perturb the membrane in a way that drives their aggregation. Such membrane-mediated forces include capillary (domain boundary) forces, which only arise under specific conditions, or lipid depletion forces, which are effective only in the subnanometric range.[9,10] Membrane perturbations may also arise from generic properties of the particles, such as their size or shape, and have been studied by computer simulation. Transmembrane proteins whose height is mismatched with the width of the surrounding membrane have also been found to aggregate if they are sufficiently large.[11] Similarly, highly curved nanoparticles, but not shallow ones,[12] adsorbed to a membrane also aggregate and, subsequently, cause it to invaginate.[13]

Here, we have used computer simulations to explore the clustering of STxB molecules and compared their predictions to fluorescence correlation spectroscopy (FCS) experiments on model membranes and live cells. We find that conventional membrane-mediated forces cannot explain the observed STxB clustering. Indeed, well-explored mechanisms such as lipid-chain length mismatch and compositional mismatch between the local membrane environment near the toxin particles and the bulk membrane were not required for STxB clustering. Nor was the hydrophobic core of the membrane affected by bound STxB. Furthermore, using atomistic molecular dynamics simulations, we recently obtained evidence that suggests that membrane-bound STxB creates a small increment of curvature,[14] which would be expected to yield a repulsive force between toxin molecules.[12,15] However, our simulations and experiments show that reducing the rigidity of the bound STxB nanoparticles or displacing them from the membrane surface eliminates the clustering process. Strikingly, this effect is paralleled by a loss of STxB nanoparticle-mediated suppression of membrane fluctuations, strongly suggesting that fluctuation-induced forces generate an effective attraction between the STxB nanoparticles. This clustering mechanism is *generic* and should operate between any sufficiently rigid nanoparticles that are able to bind tightly to a fluid phase lipid bilayer, pointing to a route for the therapeutic delivery of nanoparticles into cells.

RESULTS

FCS Setup To Measure STxB Clustering. Membrane-bound STxB was studied in a micropipette aspiration setup that provides control over membrane tension in a model membrane system, giant unilamellar vesicles (GUVs), while simultaneously allowing the analysis of clustering of membrane constituents by fluorescence correlation spectroscopy (FCS) (Figure 1A). GUVs (95 mol % 1,2-dioleoyl-*sn*-glycero-3-phosphocholine (DOPC)) were prepared by electroformation[16] with 5 mol % of a natural long chain Gb3 species, C22:1, which has previously been shown to favor STxB-driven membrane bending.[6] Stretching the membrane to high values of approximately 10^{-3} N/m provided us with two advantages in precisely testing the extent of STxB clustering. First, STxB-induced formation of tubular membrane invaginations was prevented, which allowed us to compare the different lipid species used in our experiments, independent of their ability to support tubulation. Second, stretching the membrane suppressed high amplitude membrane fluctuations that would otherwise have resulted in non-STxB diffusion related intensity fluctuations in the FCS measurements. Thereby, the

DOI: 10.1021/acsnano.6b05706
ACS Nano 2017, 11, 314−324

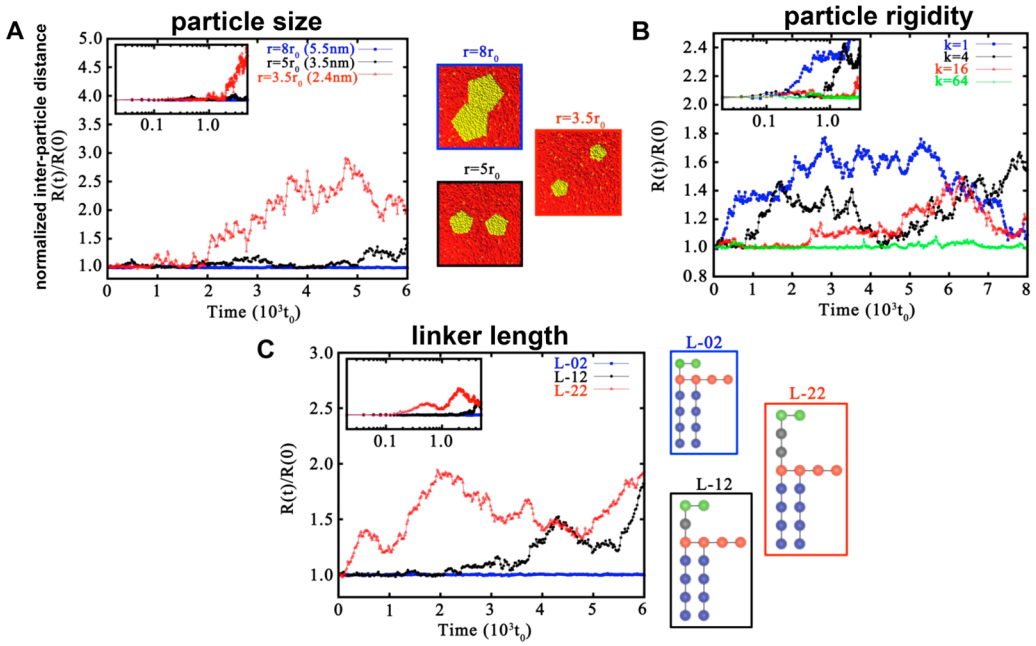

Figure 2. DPD simulations of particles on a fluctuating membrane. $R(t)$ is the distance between the centers of the NPs, and $R(0)$ is the distance between NPs at time 0. At time 0, NPs are forced to cluster, and evolution of $R(t)/R(0)$ as a function of time is measured once this external constraint is removed. (A) $R(t)/R(0)$ for different particle sizes. r_0 is the DPD length scale of 0.69 nm. (B) $R(t)/R(0)$ for different rigidity parameters k of the particles. (C) $R(t)/R(0)$ for bilayers containing different lipid structures (L-02, L-12, L-22). The boxes on the right show the respective structures used for increasing flexible linker lengths.

fluorescence intensity fluctuations observed in our experiments were predominantly due to diffusion of STxB-Alexa488 molecules in and out of the cross section of the membrane within the focal FCS observation spot. Diffusion time distributions were measured by fitting the autocorrelation curves using the maximum entropy method-based fitting routine (MEMFCS).[17] This allowed us to deduce the size distribution of the diffusing STxB clusters independent of the dimensionality of the equation used in the fitting process (Supporting Information, Figure SI15) and the photophysics of the dye (Supporting Information, Figure SI16). We found that the peak of the distribution of the diffusion times shifts with time to higher values and the distribution broadens (expressed as τ_D in Figure 1C,D). These observations suggest that the peak size of the STxB clusters as well as the size heterogeneity grew with time.

Line Tension Is Not Required for STxB Clustering. Next we exploited the above experimental setup to test whether commonly understood membrane-mediated forces can explain STxB clustering.

Lipid chain length mismatch can be very effective for driving lipid phase segregation. By creating a locally distinct lipid phase environment, STxB could aggregate through a capillary effect.[9] This possibility was addressed in our setup by using C18:1 Gb3 species whose chain length matched that of the bulk membrane lipid DOPC. Even under these conditions, STxB still clustered efficiently (Figure 1D), demonstrating that lipid chain length mismatch is not strictly required.

Compositional mismatch is another mechanism for line-tension driven clustering. We therefore tested GUVs with a bulk Gb3 concentration of 30 mol %, mimicking the estimated Gb3 concentration bound under STxB molecules[14] (see Supporting Information for further details). STxB still formed invaginations at 37 °C, above the phase transition temperature for 30% Gb3 and 70% DOPC (Figure 1B), indicating that clustering is maintained and that lipid compositional mismatch is not required. These results lead us to conclude that conventional line tension-based mechanisms are not an obligatory requirement for STxB clustering.

No Impact of STxB on the Hydrophobic Bulk of the Bilayer. Since STxB, via its receptor, Gb3, is connected to the hydrophobic region of the bilayer, one might suspect that the bound proteins modify the lipid chain entropy thereby driving their clustering. To address this possibility, we reanalyzed trajectories from our previously published work[14,18] and observed no major differences in the lipid chain order parameter (Supporting Information, Figure SI10) nor the rotational correlation function of DOPC lipids under STxB (Supporting Information, Figure SI11), when compared to DOPC lipids far from STxB. Also, when the chain order parameter of Gb3 bound to STxB was compared to that of unbound Gb3, no evidence for STxB-induced ordering could be observed (see Supporting Information, Figure SI12). Therefore, an entropic effect of STxB on the hydrophobic region of the bilayer as a source of clustering appears highly unlikely.

Local Curvature Induced by STxB Does Not Drive Clustering. Shiga toxin induces negative local membrane curvature, since it results in macroscopic membrane invagination on GUVs (see Römer et al.[6]) and membrane bending *in silico*.[14] The question thus arises whether such a curvature imprint can generate an attractive force. Indeed, for highly curved particles, an attractive curvature-induced force has been described previously.[13] Later, the same authors performed a more precise evaluation of the range of the curvature imprint for which the curvature-induced force is attractive.[12] Notably, it was found that for contact angles up to 45°, the curvature-induced force is described well by the linear approximation and is predicted to be repulsive.[12,15] STxB clearly falls into this category with a low contact angle around 7°, resulting from a

DOI: 10.1021/acsnano.6b05706
ACS Nano 2017, 11, 314–324

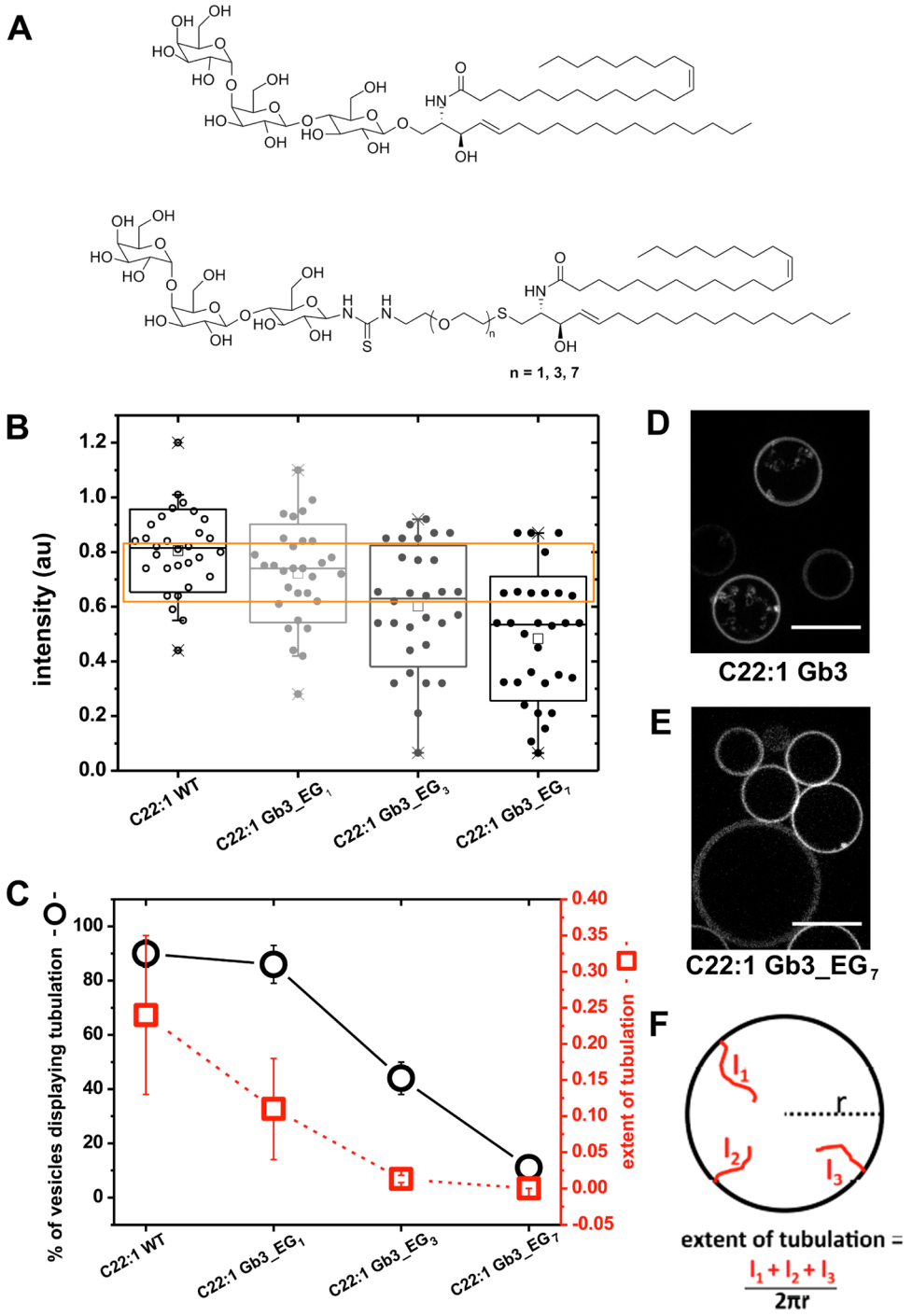

Figure 3. STxB clustering on GUVs containing Gb3 species with flexible linkers. (A) Molecular structure of the different lipids used in this study. (B) Binding of 200 nM STxB-Alexa488 to vesicles prepared with 5% mentioned Gb3 species and 95% DOPC. The yellow rectangle depicts the range within which FCS measurements were taken. (C) The percentage of vesicles displaying tubulation decreases with increasing linker length (black circles). The extent of tubulation (red boxes), that is, the sum of length of all the invaginations for a given vesicle divided by the circumference in that particular cross section (schematic in panel F), also decreases with increasing linker length. (D) An example snapshot of vesicles containing C22:1 Gb3 showing extensive tubulation. (E) An example snapshot of vesicles prepared with C22:1 Gb3_EG$_7$ showing almost no tubulation. (F) Schematic describing the measurement of extent of tubulation (see panel C). Scale bars for panels D and E, 10 μm.

spontaneous curvature radius that is 5-fold bigger than the protein's size.[14] We can therefore exclude induced membrane curvature as the driving force for STxB clustering.

Coarse-Grained Simulations of Clustering. The experimental results so far suggest that the clustering of STxB molecules is independent of the precise molecular structure of the membrane, and cannot be explained by known membrane-mediated clustering mechanisms. To proceed further, we used a coarse-grained simulation technique, dissipative particle dynamics (DPD), to study the clustering of nanoparticles (NP) that mimic the physical properties (but not the molecular details) of Shiga toxin on an amphiphilic bilayer.

DOI: 10.1021/acsnano.6b05706
ACS Nano 2017, 11, 314–324

Previous studies have shown that DPD simulations of lipid bilayers faithfully reproduce membrane physical properties, such as area per lipid and membrane elasticity for single[19] and multicomponent bilayers.[20,21] After confirming that our simulations replicated these properties (not shown), we added nanoparticles to the simulation whose shape (pentagonal), size (7 nm cross-sectional size), and material properties (high stiffness) mimic those of STxB. The detailed procedure is described in the Supporting Information, including how NP stiffness is quantified by a "rigidity parameter" k. The STxB binding to Gb3 was modeled as a nonspecific attraction between the lipid head groups and the nanoparticles. The simulated STxB nanoparticles are large enough that atomic features of their binding, including H-bonding, need not be explicitly represented, which makes DPD a suitable simulation technique. Our results are therefore robust against the details of the force field used and depend only on generic properties of the particles that are independent of their detailed molecular structure. We eliminated the possibility that clusters arise from direct binding between nanoparticles by giving them a short-range (smaller than the particle radius) *repulsive* interfacial interaction. Furthermore, height and compositional mismatch and curvature were excluded by choosing conditions in which, respectively, all lipid tails are of the same length, the NPs are flat, and the same molecular lipid species are used throughout (Supporting Information, Figure SI8B,C).

The DPD simulations showed (see Supporting Information, Movie 1) that two rigid toxin NPs initially placed apart on the membrane approached each other whereupon they adhered dependent on the stiffness and the size of the toxin NPs, as described below. Repeated simulations confirmed that, once bound, NPs did not separate for at least 9.6 μs (Figure 2A, $r = 8r_0$ condition, blue trace/box where r_0 is the unit of length in the DPD simulations and is defined in the Supporting Information). For comparison, the NPs diffuse a distance equal to their diameter in approximately 10 μs (Supporting Information, Figure SI8-A) indicating that the toxin NPs have overcome the entropic separation tendency and adhere. Strikingly, toxin NPs dampened the membrane's thermal fluctuations in our DPD simulations (Supporting Information, Figure SI7A, $k = 64$, blue dot; Figure SI7B for lipid L-02; see Supporting Information for details on the method to calculate the suppression of membrane fluctuations). This effect on fluctuations will be followed up throughout all subsequent experiments and its relevance to the clustering process addressed in the Discussion.

Why Do Not All Proteins Cluster? The above clustering mechanism might be thought to operate among all membrane-associated proteins, which would contradict the experimental observation that many membrane proteins do not cluster.[22−24] The clustering mechanism must therefore depend on properties that are not shared by all membrane proteins but that are present when the NPs in the DPD simulations bind to the membrane, for example, NP size, geometry, stiffness, and coupling to the membrane.

In a first set of simulations, we found that NPs with sizes similar to that of the NP from Supporting Information, Movie 1, but with different geometries (square, hexagonal, and disk-like), aggregated on tense or tensionless bilayers (not shown). These results demonstrate that the membrane tension and NP shape do not remove the clustering although the force may be altered. By contrast, we found that clustering disappeared when the nanoparticle diameter was less than about 2.5 nm (Figure 2A, red trace; Supporting Information, Movies 2−4).

We next modified the internal stiffness of the NPs to explore the effects of their rigidity and found that clustering vanished for values of the rigidity parameter $k = 16$ or below (Figure 2B). This result is in agreement with that found in Monte Carlo simulations of inclusions on a fluctuating surface by Weikl.[25] The suppression of membrane fluctuations was no longer observed in conditions under which a loss of rigidity led to a loss of clustering (Supporting Information, Figure SI7A). We also note that solvent depletion forces are still present for highly flexible NPs, demonstrating that these were not sufficient for clustering.

These results showed that clustering in DPD simulations is strongly dependent on the NP size and internal rigidity. Unfortunately, neither of these properties can be modified experimentally in the STxB system. However, the mechanical coupling of a NP onto the bilayer is experimentally accessible and was therefore addressed next.

STxB Clustering Requires Tight Mechanical Coupling to the Membrane. To test the importance of *tight* mechanical coupling between NPs and membrane, we added flexible linker segments (gray beads in the schematics of Figure 2C) of increasing length (L-12 or L-22 carry 1 or 2 linker beads, respectively) to the lipid head groups (red beads). In this DPD simulation, distal regions (green beads) remained attractive to the toxin NPs, which therefore adsorbed to the membrane in all cases. When toxin NPs were forced to aggregate, they separated again when linkers were longer than 1 nm (Figure 2C, L-12 and L-22 conditions; black and red traces/boxes, respectively; Supporting Information, Movies 5 and 6), whereas they remained bound for up to 4.8 μs in all simulations in the absence of any flexible linker segments (Figure 2C, L-02 condition, blue trace/box). Importantly, the loss of clustering with increasing linker length again correlated with the loss of suppression of membrane fluctuations (Supporting Information, Figure SI7B), pointing to the possibility of a causal link between fluctuations and clustering (see Discussion).

We returned to the GUV/FCS setup to test experimentally how soft linkers influence STxB clustering. For this, we synthesized three artificial Gb3 species: C22:1 Gb3_EG$_n$, in which the globotriose sugar headgroup was separated from the ceramide backbone by 1, 3, or 7 ethylene glycol (EG) units (Figure 3A), corresponding to 1.0, 1.75, or 3.25 nm of extended linker length. Details of the chemical synthesis can be found in the Supporting Information. GUVs were prepared with these artificial Gb3 species, as described above. The binding of STxB was similar in all cases (Figure 3B). By contrast, there was a marked difference in the ability to form inward tubules (Figure 3C, black circles, D, and E), and the extent of tubulation (Figure 3F) was clearly reduced with increasing linker length (Figure 3C, red boxes).

Using FCS on micropipette aspirated GUVs for which tubulation was suppressed by tensing the membranes allowed us to precisely compare the extent of STxB clustering for all lipids. Compared to the natural C22:1 Gb3 species, STxB clustering kinetics was already slightly reduced on C22:1 Gb3_EG$_1$ (Figure 4). For Gb3_EG$_3$ and Gb3_EG$_7$, no significant aggregation was observed as τ_D did not extend beyond 20 ms and the width of τ_D distribution remained comparable with time (Figure 4). Whereas clusters formed from natural Gb3 have hydrodynamic radii of 180 nm, estimated as described in Supporting Information, those

DOI: 10.1021/acsnano.6b05706
ACS Nano 2017, 11, 314−324

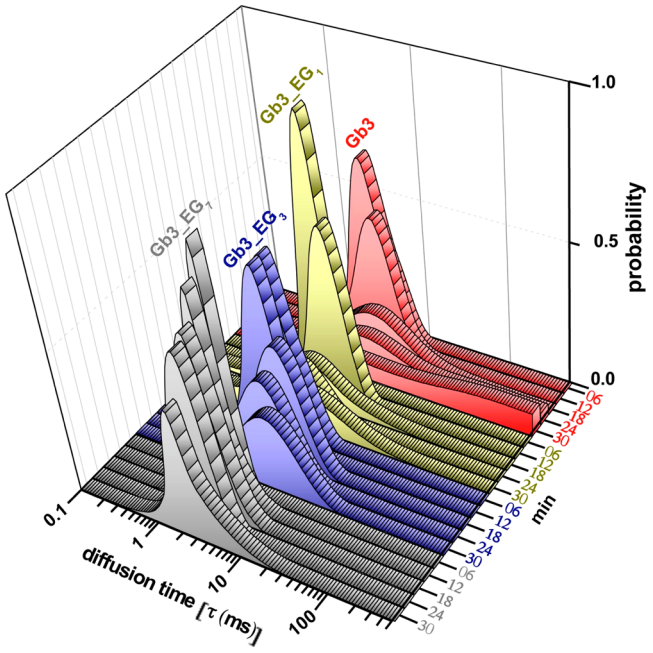

Figure 4. Clustering experiments on GUVs using Gb3 species with flexible linkers. Distributions of lifetimes for 200 nM STxB-Alexa488 on tensed GUVs obtained from MEMFCS fitting for different lipids as a function of time. On GUVs with C22:1 Gb3, STxB shows increased clustering at longer time scales. STxB clustering on C22:1 Gb3_EG$_3$ and C22:1 Gb3_EG$_7$ linker containing GUVs was strongly reduced.

formed from Gb3_EG$_3$ and Gb3_EG$_7$ have a hydrodynamic radius that remains below 10 nm, which is comparable to the size of a single STxB particle. These results closely mirror the ones made with soft linkers in DPD simulations (Figure 2C) and suggest a systematic decrease in the degree of clustering, related to the ethylene glycol linker lengths between the head and tail groups of the corresponding Gb3 species. Since the density of toxins at the cell surface is similar in all conditions, our findings further support the absence of direct protein−protein interactions between STxB molecules. These experiments provide evidence that tight mechanical coupling onto the membrane is essential for STxB clustering.

To examine if flexible EG linkers also affected STxB clustering on cellular membranes, we incorporated synthetic C18:1 Gb3 or C18:1 Gb3_EG$_7$ species into GSL-deficient GM95 cells. We first showed that the binding of the toxin on the cells incorporated with these lipids was similar (Figure 5A,B). Consistent with the experiments on GUVs, we found using FCS measurements that STxB clustering was strongly compromised on cells with C18:1 Gb3_EG$_7$ species (Figure 5C,D,E).

We finally exploited phosphine-based quenching to differentiate internalized STxB from plasma membrane-accessible extracellular STxB. Using this approach, we found that the endocytic uptake of STxB was strongly reduced on cells that were reconstituted with C18:1 Gb3_EG$_7$ species, when compared to cells that were reconstituted with natural C18:1 Gb3 (Figure 6A,B). Both the number of STxB-positive endosomes per cell and the breadth of STxB fluorescence intensity distribution were strongly reduced in the C18:1 Gb3_EG$_7$ condition.

Thus, the mechanical coupling of STxB to the plasma membrane and its capacity to cluster were of critical importance to its efficient uptake into cells.

DISCUSSION

Clustering of the bacterial Shiga toxin on the cellular plasma membrane is required for infection of the cell. Several

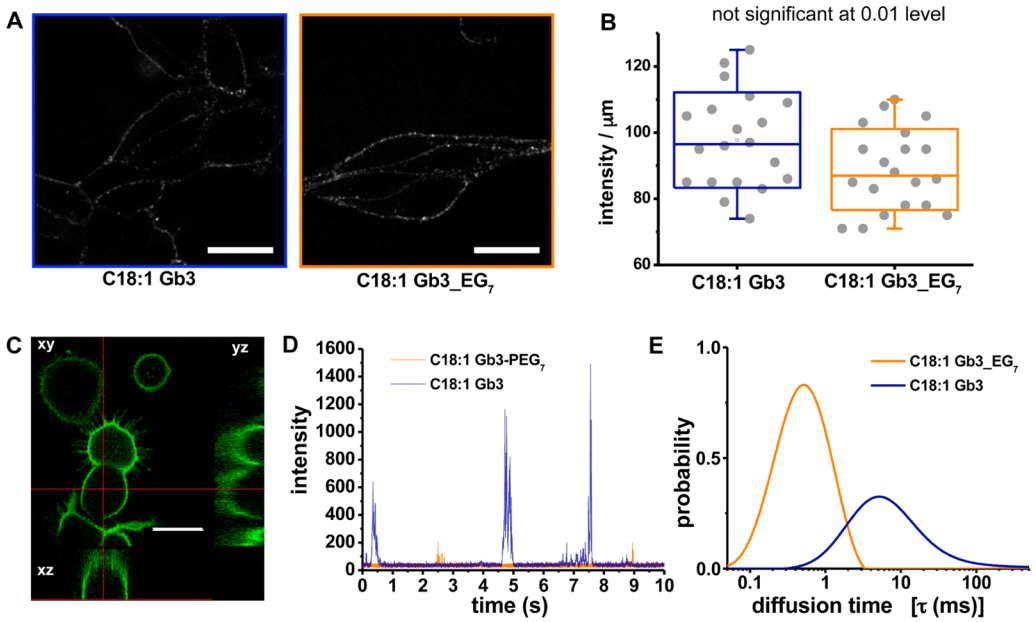

Figure 5. Binding of STxB to GM95 cells reconstituted with C18:1 Gb3 or C18:1 Gb3_EG$_7$. (A) Incubation on ice of correspondingly reconstituted cells with 200 nM STxB-Alexa488. (B) Average intensity per micrometer is similar for cells incorporated with both lipid species. Two-sample *t* test. (C) A representative image of cells incorporated with C18:1 Gb3 and incubated with STxB-Alexa488. FCS measurements were performed at the dorsal plasma membrane domain. Ten autocorrelation curves were obtained from 3 different cells for each condition and averaged for MEMFCS analysis. (D) A representative plot of intensity as a function of time for C18:1 Gb3_EG$_7$ (orange) and C18:1 Gb3 (blue). (E) The distributions of τ_D for the different lipids. Scale bars 10 μm.

DOI: 10.1021/acsnano.6b05706
ACS Nano 2017, 11, 314−324

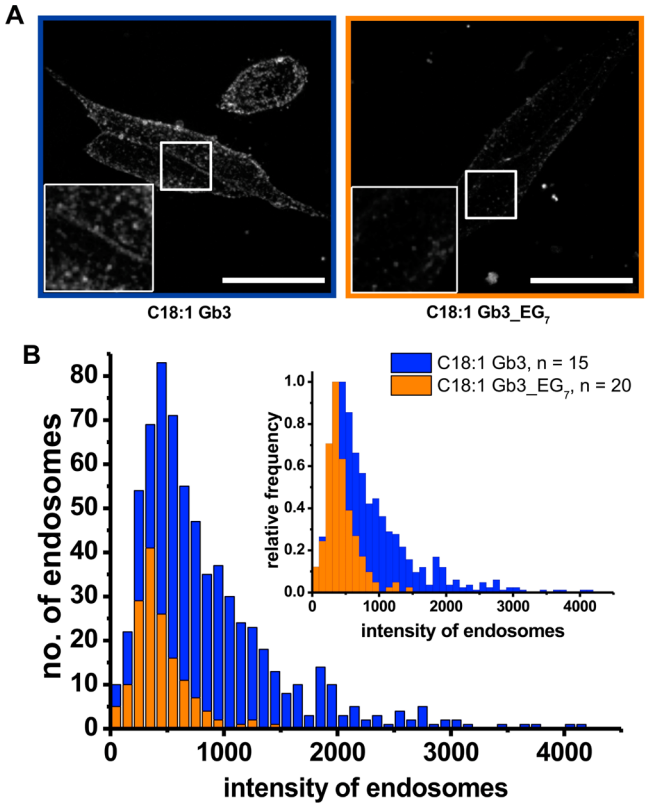

Figure 6. STxB endocytosis efficiency is dependent on flexible linker length. (A) Example images of cells fixed after 10 min of incubation at 37 °C, and subsequent TCEP treatment to quench fluorescence of cell surface-exposed STxB-Cy5 prior to imaging. Inset shows zoomed views from the boxed area of cells. (B) Histogram of vesicle intensities. Inset: Normalized histogram. Vesicle intensities for C18:1 Gb3 incorporated cells are significantly higher than for C18:1 Gb3_EG$_7$ incorporated cells. Scale bar 10 μm.

mechanisms exist that could drive aggregate formation. At large length scales of 10−100 nm, the acto-myosin machinery[7] can bring the constituents together, while at the opposite limit below 1 nm, attractive interactions such as screened electrostatics, hydrogen bonding, and van der Waals forces take over.[26] In between, depletion and capillary forces[27] could act between the toxin particles and drive their aggregation.

Our experiments show that while depletion forces may always be present, they are insufficient to cause clustering. Conversely, clustering is not prevented on removing the sources of conventional capillary forces such as lipid chain length mismatch between the toxin's cognate Gb3 lipids and surrounding membrane lipids, compositional mismatch between the membrane environment under the toxin particles and surrounding regions, and a modified membrane hydrophobic region underneath the toxin. Shiga toxin clustering thus seems to be driven by a generic mechanism whose sole requirements are (1) a fluid bilayer, (2) large particle size (>3 nm), and (3) tight mechanical coupling of the toxin proteins to the membrane. What physical principle could drive this generic clustering? Because of the link of our findings to membrane fluctuations (described below), we believe that a membrane fluctuation-induced force best explains our results.

Fluctuation-induced forces were first recognized by Casimir who described the force experienced by two parallel, uncharged conductors in a vacuum that confine quantum fluctuations of the electromagnetic field.[28] Subsequently, Casimir-like forces were postulated to arise universally in structured fluids characterized by long-range fluctuations[29,30] They were originally proposed in the context of critical mixtures[31] and soon after suggested as a mechanism of attraction between membrane proteins at critical compositions.[32] A recent review describes many examples of so-called thermal Casimir forces that have fundamental and technological importance.[33] Of particular interest here is the possibility that fluctuation-induced forces arise between the membrane-adsorbed STxB particles because they suppress the thermally driven interfacial fluctuations, that is, protrusions and undulations,[34,35] of the membrane (See Supporting Information).

Such an effect has largely been ignored in the experimental biophysical literature because the first predictions of its strength between point-like membrane inclusions had suggested that it was small compared to other interactions between membrane proteins.[15,36] It was subsequently calculated to scale more strongly at short distances,[29,37,38] and we have performed further calculations using the proximity force approximation of Derjaguin[39] to estimate the force and its distance dependence for closely apposed rigid particles. These results show that it is comparable to unscreened electrostatic interactions for nanometer size inclusions (see Thermal Casimir Force section in the Supporting Information). The effective range of the thermal Casimir force is predicted to be several nanometers (i.e., comparable to the size of the nanoparticle).

We estimate from FCS experiments on highly tensed vesicles (for which invaginations cannot form) that clusters can grow into domains that are hundreds of nanometers in size (Supporting Information), indicating their phase separation into toxin-rich domains embedded in the surrounding toxin-poor membrane. When this phase separation occurs on membranes with low values of membrane tension, the small increment of curvature induced by each toxin particle, which has been predicted from atomistic Molecular Dynamics simulations[14] to be 0.035 nm^{-1}, creates a spontaneous curvature in the toxin-rich domains[40] that subsequently drives their tubular invagination,[41,42] as seen in Figure 1B.

The thermal Casimir force depends on the ability of membrane-adsorbed particles to suppress the thermal membrane fluctuations beneath them because this restricts the fluctuation spectrum of the free membrane regions and gives rise to the attractive force between the particles.[25,38,43] It was therefore of interest to note that STxB nanoparticles dampened the membrane's thermal fluctuations in our DPD simulations. Importantly, this suppression of membrane fluctuations was not observed under the same conditions in which loss of rigidity or the presence of long flexible linkers led to a loss of clustering. The thermal Casimir effect is also expected to increase with nanoparticle size and rigidity,[43,44] which agrees with our simulations.

One unintuitive aspect of the Casimir force is that it is nonadditive as pointed out in several previous studies.[45−48] The total Casimir force between any pair of particles in a many body system is still attractive and can be larger than the sum of the individual pairwise forces. Although the ratio of the many-body contribution to the sum of the pairwise forces is calculated to be negligible at large separations, it reaches a factor of 2 at small separations and therefore strengthens the attraction.[46,47]

Probing the thermal Casimir force in membranes experimentally is a challenging task. It is not possible to use the temperature or membrane tension as control parameters

DOI: 10.1021/acsnano.6b05706
ACS Nano 2017, 11, 314−324

because membranes undergo phase changes or rupture events within a relatively small range of temperatures or values of membrane tension. The relevant short-distance behavior caused by the Casimir-like force is practically insensitive to changes within this experimentally accessible regime of temperatures or membrane tension values.[29,30]

For experimental testing, we therefore exploited the fact that the thermal Casimir force arises only when membrane inclusions locally suppress membrane fluctuations,[30,43] as validated in our simulations. Using Gb3 species for which flexible linkers separate the carbohydrate part from the ceramide backbone, thus removing the suppression of the membrane fluctuations at the binding sites of the B-subunit of Shiga toxin (STxB), we could experimentally show that a tight mechanical coupling of STxB onto the membrane was required for toxin clustering. Therefore, unlike the capillary forces mentioned above, whose removal one by one did not prevent the clustering, when the conditions for the thermal Casimir force are removed (by displacing the toxin particles with the linker) the clustering is eliminated, indicating that the thermal Casimir force is essential for clustering to occur.

The thermal Casimir force hypothesis provides a fresh view of clustering processes that operate in concert on biological membranes. It is also versatile compared to mechanisms such as capillary attraction because the only constraint on the (fluid) membrane composition is the presence of an appropriate binding partner (e.g., the GSL Gb3 for STxB). We hypothesize that bacterial and viral evolution proceeding only by modifying the protein sequence of the infectious disease particles has harnessed a generic, fundamental force to initiate cellular entry that solely requires conserved binding sites for GSLs. Many pathogens and pathogenic factors bind to GSLs for their entry into cells,[49] indicating that a Casimir-like force-driven clustering mechanism may apply also to these. Furthermore, thermal Casimir interactions should occur for manufactured rigid nanoparticles that tightly adsorb onto the plasma membrane. The clustering mechanism that we describe here is therefore expected to contribute to cellular, pathogenic, and pharmaceutical drug delivery processes.

MATERIALS AND METHODS

Preparation of GUVs. 1,2-Dioleoyl-*sn*-glycero-3-phosphocholine (DOPC) was purchased from Avanti Polar Lipids (Alabaster, Alabama, USA). GUVs were prepared by electroformation.[16] One microliter of DOPC/X (X = C22:1, C22:1 Gb3_EG$_1$, C22:1 Gb3_EG$_3$, or C22:1 Gb3_EG$_7$) at 95:5 ratio at 1 mg/mL in chloroform was spread on two indium tin oxide-coated glass plate electrodes that were spaced 4 mm apart. The electrodes with the lipid films were immersed in a chamber containing 320 mM sucrose solution and were connected to a power generator. Electroformation was performed at 2 V and 10 Hz for 1 h at 65 °C. The GUVs were released from the electrodes by changing the frequency to 2 Hz for 30 min, and transferred into a chamber with equiosmolar PBS.

Micropipette Aspiration. Glass micropipettes were prepared using a Sutter P-2000 micropipette puller (Novato, USA). The glass micropipettes were passivated with β-casein at 5 mg/mL. GUVs were placed in a homemade chamber consisting of two coverslips separated by 1 mm, aspirated with a glass micropipette, and membrane tension was adjusted by changing the difference of hydrostatic pressure.[50] For each GUV used for FCS measurements, the membrane was stressed to approximately 10^{-3} N/m to minimize intensity variations contributed by the fluctuations of the membrane along the long axis of the focal spot.

Fluorescence Correlation Spectroscopy. FCS was performed using a Picoquant accessory FCS unit on a Nikon confocal scanning microscope. STxB was labeled with Alexa488 (Life Technologies), according to the manufacturers instructions. The 488 nm beam was focused on the bottom pole of the membrane, and the emission was collected from 510 to 560 nm using a dichroic mirror and a filter in front of the avalanche photodiodes. Data were collected using Symphotime64 software and exported in ASCII format for independent data analysis. Every 6 min, data were collected in run lengths of 30 s for a total duration of 30 min and then grouped. The autocorrelation curve for every recording was averaged and used for MEMFCS analysis (Supporting Information, Figure SI13).

Data Analysis. The FCS data was analyzed according to the maximum entropy method using[17]

$$G(\tau) = \sum_{i=1}^{n} a_i \left(\frac{1}{1+\tau/\tau_{D_i}}\right)\left(\frac{1}{1+\frac{\tau}{K^2\tau_{D_i}}}\right)^{1/2}$$

MEMFCS minimizes χ^2 as well as maximizes the entropic quantity, defined by $S = \sum_i p_i \ln p_i$, which then detects a distribution of diffusion times, the amplitude of which is related as $p_i = \frac{a_i}{\sum_j a_j}$ for each event. $G(0)$ corresponds to the sum of all amplitudes. By normalizing the amplitudes, the logarithmic distribution of diffusion times represents the probability that a specific noninteracting species has a particular diffusion time. Typically, the distribution maximizes at the most probable diffusion time for a single distribution. Fits were obtained by setting the number of species to 150, with the diffusion times ranging from 1×10^{-3} to 1000 ms. The fits were deemed good by the residuals for all the curves and the apparent diffusion times corresponding to photophysical processes and diffusion were verified independently by a membrane binding protein, MinD (53 kDa), labeled with Alexa488. The fact that the time scales of the photophysical processes are below 0.01 ms as expected and diffusion times of MinD peak at a few milliseconds verifies the MEMFCS fitting routine and confirms the diffusion time of monomeric STxB (Supporting Information, Figure SI16).

Incorporation of Lipids into Cell Membranes. For incorporation of lipids, GM95 cells were incubated for 48 h in serum free medium with C18:1 Gb3 or C18:1 Gb3_EG$_7$. To minimize the amount of Gb3 nonspecifically attached to cells and the glass surface, cells were washed 3 times with medium containing 10% FCS. Subsequently cells were detached with accutase, collected by centrifugation, and replated in fibronectin-coated glass bottom dishes for 60 min. Cells were incubated with 0.5 μM STxB-Alexa488 for 20 min at 37 °C, washed to remove unbound STxB, and imaged at RT. C18:1 Gb3_EG$_7$ incorporated into the plasma membrane less efficiently than C18:1 Gb3. To achieve comparable STxB-Alexa488 intensities on the plasma membrane, lipid and toxin concentration were adjusted: C18:1 Gb3 was incorporated at 3.3 μM, and C18:1 Gb3_EG$_7$ at 50 μM.

Endocytosis Assay. STxB-Cy5 was allowed to bind on ice to GM95 cells incorporated with C18:1 Gb3 or C18:1 Gb3_EG$_7$ for 15 min in DMEM buffer supplemented with HEPES at 25 mM. Cells were shifted for 10 min to 37 °C and fixed with 4% PFA in phosphate buffer. To quench the fluorescence of membrane bound, non-internalized STxB-Cy5, samples were imaged in a buffer containing 0.2 M Tris at pH 9, 100 mM TCEP, 5% glucose, 1 mM ascorbic acid, and an oxygen scavenging system consisting of 0.5 mg/mL glucose oxidase, 40 μg/mL catalase, and 5% glucose.[51] Exposing to 633 nm laser quenched all extracellular STxB-Cy5 and allowed distinguished imaging of endocytosed STxB-Cy5 (Supporting Information, Figure SI14). Quantification of endocytosis efficiency on cells reconstituted with C18:1 Gb3 or C18:1 Gb3_EG$_7$ was carried out with a custom MATLAB software that identifies and measures the intensity of individual endosomes.

Simulation Methods. The details of the dissipative particle dynamics simulations and the model for proteins in these simulations, as well as the force field parameters in which proteins suppress membrane fluctuations, can be found in the Supporting Information.

DOI: 10.1021/acsnano.6b05706
ACS Nano 2017, 11, 314−324

Lipid Synthesis. The extensive reaction schemes are described in the Supporting Information.

ASSOCIATED CONTENT

Supporting Information

In the associated Supporting Information we provide movies that show the results of the DPD and MD simulations, and detailed descriptions of our experimental and theoretical work as described below. The Supporting Information is available free of charge on the ACS Publications website at DOI: 10.1021/acsnano.6b05706.

Description of the thermal Casimir force between membrane inclusions as presented in the literature and our calculations using the proximity force approximation of the thermal Casimir force between a pair of polygonal particles at separations that are small compared to their size, the dissipative particle dynamics simulations of nanoparticles adsorbed to a fluctuating membrane, showing that only when the nanoparticles suppress the membrane fluctuations do they experience a clustering force, reanalysis of trajectories from our previously published molecular dynamics (MD) simulations[14,18] showing that the binding of STxB to the membrane does not change the lipids' chain order parameter nor their rotational diffusion, experimental protocol for adding the STxB toxin particles to the vesicles and cells, estimation of the membrane coverage due to STxB binding to Gb3 lipids, FCS experiments that are used to measure the decrease in diffusion as the toxin nanoparticles aggregate, and complete organic synthesis reactions for the PEG-modified Gb3 lipids (PDF)

Movie 1, flat pentagonal NPs with radius R = 5.5 nm attract after adhesion to the bilayer surface and remain attached to each other until the end of the simulation (AVI)

Movie 2, flat pentagonal NPs with radius R = 2.4 nm are forced to aggregate and after the force is removed (starting configuration of the system) start to separate immediately (AVI)

Movie 3, flat pentagonal NPs with radius R = 3.5 nm are forced to aggregate and after the force is removed (starting configuration of the system) are still attached to each other for about 4 μs (AVI)

Movie 4, flat pentagonal NPs with radius R = 5.5 nm are forced to aggregate and after the force is removed (starting configuration of the system) are still attached to each other for at least 9.6 μs (AVI)

Movie 5, flat pentagonal NPs with radius R = 5.5 nm adhere to a bilayer composed of the lipid with structure L-12, are forced to aggregate, and after the force is removed (starting configuration of the system) are attached to each other for about 2.5 μs (AVI)

Movie 6, flat pentagonal NPs with radius R = 5.5 nm adhere to a bilayer composed of the lipid with structure L-22, are forced to aggregate, and after the force is removed (starting configuration of the simulation) start to separate immediately (AVI)

Movie 7, spherical NPs with pentagonal base adhered to a bilayer composed of the lipid with shown in Figure SI2-1 are forced to aggregate and after the force is removed (starting configuration of the simulation) start to separate immediately showing that curvature energy does not mediate an attractive force (AVI)

Movie 8, spherical NPs with pentagonal base adhered to a bilayer composed of the lipid with shown in Figure SI2-1 are forced to aggregate and after the force is removed (starting configuration of the simulation) start to separate immediately showing that curvature energy does not mediate an attractive force (AVI)

Movie 9, 200 ns all-atom MD simulation of a STxB protein bound to a membrane from a trajectory of our previously published paper[20] (AVI)

AUTHOR INFORMATION

Corresponding Authors

*ipsen@memphys.sdu.dk
*ludger.johannes@curie.fr
*julian.shillcock@epfl.ch

ORCID

Julian C. Shillcock: 0000-0002-7885-735X

Author Contributions

°W.P., H.G., and S.A. contributed equally. J.H.I., L.J., and J.C.S. are principal investigators. J.C.S., J.H.I., and L.J. conceived the study. W.P., J.H.I., and J.C.S. developed and performed the DPD simulations. H.G. and J.C.F. designed and synthesized the lipids. S.A. designed and performed FCS experiments and analyzed data. S.A. and U.B. performed *in vivo* experiments. P.B. gave technical support and conceptual advice. S.A., L.J., J.H.I., W.P., and J.C.S. wrote the main paper. All authors discussed the results and commented on the manuscript at all stages.

Notes

The authors declare no competing financial interest.

ACKNOWLEDGMENTS

We thank M. Deserno, L. Monticelli, and A. Imparato for instructive discussions. The research leading to these results has received funding from the European Community's Seventh Framework Programme (FP7/2007-2013) under grant agreement number TRANSPOL-264399 to L.J. and J.H.I. This work was supported by grants from the Agence Nationale pour la Recherche (ANR-09-BLAN-283 to LJ and ANR-11 BSV2 014 03 to LJ & PB), Human Frontier Science Program grant RGP0029-2014 to L.J. and J.H.I., European Research Council advanced grant (project 340485, L.J.), and by a fellowship from Fondation ARC pour la Recherche sur le Cancer (H.G.). The Johannes and Bassereau teams are members of Labex CelTisPhyBio (11-LBX-0038) and Idex Paris Sciences et Lettres (ANR-10-IDEX-0001-02 PSL). S.A. acknowledges a fellowship from Fondation Pierre-Gilles de Gennes. Simulations for the work described in this paper were performed using resources provided by the DeiC National HPC Centre, University of Southern Denmark. The facilities as well as scientific and technical assistance from staff in the PICT-IBiSA/Nikon Imaging Centre at Institut Curie-CNRS and the France-BioImaging infrastructure (ANR-10-INSB-04) are acknowledged.

REFERENCES

(1) Karch, H.; Denamur, E.; Dobrindt, U.; Finlay, B. B.; Hengge, R.; Johannes, L.; Ron, E. Z.; Tønjum, T.; Sansonetti, P. J.; Vicente, M. The Enemy within Us: Lessons from the 2011 European Escherichia Coli O104:H4 Outbreak. *EMBO Mol. Med.* **2012**, *4*, 841−848.

(2) Johannes, L.; Römer, W. Shiga toxins - from Cell Biology to Biomedical Applications. *Nat. Rev. Microbiol.* **2010**, *8*, 105−116.

DOI: 10.1021/acsnano.6b05706
ACS Nano 2017, 11, 314−324

(3) Bergan, J.; Dyve Lingelem, A. B.; Simm, R.; Skotland, T.; Sandvig, K. Shiga Toxins. *Toxicon* **2012**, *60*, 1085−1107.
(4) Johannes, L.; Parton, R. G.; Bassereau, P.; Mayor, S. Building Endocytic Pits without Clathrin. *Nat. Rev. Mol. Cell Biol.* **2015**, *16*, 311−321.
(5) Spooner, R. A.; Lord, J. M. How Ricin and Shiga Toxin Reach the Cytosol of Target Cells: Retrotranslocation from the Endoplasmic Reticulum. *Curr. Top. Microbiol. Immunol.* **2012**, *357*, 19−40.
(6) Römer, W.; Berland, L.; Chambon, V.; Gaus, K.; Windschiegl, B.; Tenza, D.; Aly, M. R.; Fraisier, V.; Florent, J.-C.; Perrais, D.; Lamaze, C.; Raposo, G.; Steinem, C.; Sens, P.; Bassereau, P.; Johannes, L. Shiga Toxin Induces Tubular Membrane Invaginations for Its Uptake into Cells. *Nature* **2007**, *450*, 670−675.
(7) Rao, M.; Mayor, S. Active Organization of Membrane Constituents in Living Cells. *Curr. Opin. Cell Biol.* **2014**, *29*, 126−132.
(8) Raghupathy, R.; Anilkumar, A. A.; Polley, A.; Singh, P. P.; Yadav, M.; Johnson, C.; Suryawanshi, S.; Saikam, V.; Sawant, S. D.; Panda, A.; Guo, Z.; Vishwakarma, R. A.; Rao, M.; Mayor, S. Transbilayer Lipid Interactions Mediate Nanoclustering of Lipid-Anchored Proteins. *Cell* **2015**, *161*, 581−594.
(9) Gil, T.; Ipsen, J. H. Capillary Condensation Between Disks in Two Dimensions. *Phys. Rev. E: Stat. Phys., Plasmas, Fluids, Relat. Interdiscip. Top.* **1997**, *55*, 1713−1721.
(10) Sintes, T.; Baumgartner, A. Protein Attraction in Membranes Induced by Lipid Fluctuations. *Biophys. J.* **1997**, *73*, 2251−2259.
(11) Schmidt, U.; Guigas, G.; Weiss, M. Cluster Formation of Transmembrane Proteins Due to Hydrophobic Mismatching. *Phys. Rev. Lett.* **2008**, *101*, 128104.
(12) Reynwar, B. J.; Deserno, M. Membrane-Mediated Interactions Between Circular Particles in the Strongly Curved Regime. *Soft Matter* **2011**, *7*, 8567−8575.
(13) Reynwar, B. J.; Illya, G.; Harmandaris, V. A.; Muller, M. M.; Kremer, K.; Deserno, M. Aggregation and Vesiculation of Membrane Proteins by Curvature-Mediated Interactions. *Nature* **2007**, *447*, 461−464.
(14) Pezeshkian, W.; Hansen, A. G.; Johannes, L.; Khandelia, H.; Shillcock, J. C.; Kumar, P. B.; Ipsen, J. H. Membrane Invagination Induced by Shiga Toxin B-Subunit: from Molecular Structure to Tube Formation. *Soft Matter* **2016**, *12*, 5164−5171.
(15) Goulian, M.; Bruinsma, R.; Pincus, P. Long-Range Forces in Heterogeneous Fluid Membranes. *Europhys. Lett.* **1993**, *22*, 145−150.
(16) Angelova, M. I.; Dimitrov, D. S. Liposome Electroformation. *Faraday Discuss. Chem. Soc.* **1986**, *81*, 303−311.
(17) Sengupta, P.; Garai, K.; Balaji, J.; Periasamy, N.; Maiti, S. Measuring Size Distribution in Highly Heterogeneous Systems with Fluorescence Correlation Spectroscopy. *Biophys. J.* **2003**, *84*, 1977−1984.
(18) Pezeshkian, W.; Chaban, V. V.; Johannes, L.; Shillcock, J.; Ipsen, J. H.; Khandelia, H. The Effects of Globotriaosylceramide Tail Saturation Level on Bilayer Phases. *Soft Matter* **2015**, *11*, 1352−1361.
(19) Shillcock, J. C.; Lipowsky, R. Equilibrium Structure and Lateral Stress Distribution of Amphiphilic Bilayers from Dissipative Particle Dynamics Simulations. *J. Chem. Phys.* **2002**, *117*, 5048−5061.
(20) Laradji, M.; Sunil Kumar, P. B. Domain Growth, Budding, and Fission in Phase-Separating Self-Assembled Fluid Membranes. *J. Chem. Phys.* **2005**, *123*, 224902−2249011.
(21) Illya, G.; Lipowsky, R.; Shillcock, J. C. Two-Component Membrane Material Properties and Domain Formation from Dissipative Particle Dynamics. *J. Chem. Phys.* **2006**, *125*, 114710−114718.
(22) van den Bogaart, G.; Meyenberg, K.; Risselada, H. J.; Amin, H.; Willig, K. I.; Hubrich, B. E.; Dier, M.; Hell, S. W.; Grubmuller, H.; Diederichsen, U.; Jahn, R. Membrane Protein Sequestering by Ionic Protein-Lipid Interactions. *Nature* **2011**, *479*, 552−555.
(23) Garcia-Saez, A. J.; Ries, J.; Orzaez, M.; Perez-Paya, E.; Schwille, P. Membrane Promotes tBID Interaction with BCL(XL). *Nat. Struct. Mol. Biol.* **2009**, *16*, 1178−1185.
(24) Sorre, B.; Callan-Jones, A.; Manzi, J.; Goud, B.; Prost, J.; Bassereau, P.; Roux, A. Nature of Curvature Coupling of Amphiphysin with Membranes Depends on its Bound Density. *Proc. Natl. Acad. Sci. U. S. A.* **2012**, *109*, 173−178.
(25) Weikl, T. R. Dynamic Phase Separation of Fluid Membranes with Rigid Inclusions. *Phys. Rev. E: Stat. Phys., Plasmas, Fluids, Relat. Interdiscip. Top.* **2002**, *66*, 061915.
(26) Israelachvili, J. *Intermolecular and Surface Forces*, 2nd ed.; Academic Press: London, 1992.
(27) Lehle, H.; Noruzifar, E.; Oettel, M. Ellipsoidal Particles at Fluid Interfaces. *Eur. Phys. J. E: Soft Matter Biol. Phys.* **2008**, *26*, 151−160.
(28) Casimir, H. B. G.; Polder, D. The Influence of Retardation on the London-Vanderwaals Forces. *Phys. Rev.* **1948**, *73*, 360−372.
(29) Li, H.; Kardar, M. Fluctuation-Induced Forces Between Manifolds Immersed in Correlated Fluids. *Phys. Rev. A: At., Mol., Opt. Phys.* **1992**, *46*, 6490−6500.
(30) Kardar, M.; Golestanian, R. The "Friction" of Vacuum, and other Fluctuation-Induced Forces. *Rev. Mod. Phys.* **1999**, *71*, 1233−1245.
(31) Fisher, M. E.; de Gennes, P. G. Wall Phenomena in a Critical Binary Mixture. *C. R. Seances Acad. Sci. Ser. B* **1978**, *287*, 207−209.
(32) Sackmann, E. Physical Basis for Trigger Processes and Membrane Structures. In *Biological Membranes*; Chapman, D., Ed.; Academic Press: London, 1987; Vol. *5*, pp 105−143.
(33) Woods, L. M.; Dalvit, D. A. R.; Tkatchenko, A.; Rodriguez-Lopez, P.; Rodriguez, A. W.; Podgornik, R. Materials Perspective on Casimir and van der Waals Interactions. *Rev. Mod. Phys.* **2016**, *88*, 045003.
(34) Park, J. M.; Lubensky, T. C. Interactions Between Membrane Inclusions on Fluctuating Membranes. *J. Phys. I* **1996**, *6*, 1217−1235.
(35) Goulian, M. Inclusions in Membranes. *Curr. Opin. Colloid Interface Sci.* **1996**, *1*, 358−361.
(36) Yolcu, C.; Deserno, M. Membrane-Mediated Interactions Between Rigid Inclusions: an Effective Field Theory. *Phys. Rev. E* **2012**, *86*, 031906.
(37) Golestanian, R.; Goulian, M.; Kardar, M. Fluctuation-Induced Interactions Between Rods on Membranes and Interfaces. *Europhys. Lett.* **1996**, *33*, 241−246.
(38) Lin, H. K.; Zandi, R.; Mohideen, U.; Pryadko, L. P. Fluctuation-Induced Forces Between Inclusions in a Fluid Membrane Under Tension. *Phys. Rev. Lett.* **2011**, *107*, 228104.
(39) Derjaguin, B. V.; Abrikosova, I. I.; Lifshitz, E. M. Direct Measurement of Molecular Attraction Between Solids Separated by a Narrow Gap. *Q. Rev., Chem. Soc.* **1956**, *10*, 295−329.
(40) Lipowsky, R. Spontaneous Tubulation of Membranes and Vesicles Reveals Membrane Tension Generated by Spontaneous Curvature. *Faraday Discuss.* **2013**, *161*, 305−331.
(41) Liu, Y.; Agudo-Canalejo, J.; Grafmuller, A.; Dimova, R.; Lipowsky, R. Patterns of Flexible Nanotubes Formed by Liquid-Ordered and Liquid-Disordered Membranes. *ACS Nano* **2016**, *10*, 463−474.
(42) Lipowsky, R. Remodeling of Membrane Compartments: Some Consequences of Membrane Fluidity. *Biol. Chem.* **2014**, *395*, 253−274.
(43) Golestanian, R. Reduced Persistence Length and Fluctuation-Induced Interactions of Directed Semiflexible Polymers on Fluctuating Surfaces. *Europhys. Lett.* **1996**, *36*, 557−561.
(44) Bimonte, G.; Emig, T.; Kardar, M. Conformal Field Theory of Critical Casimir Interactions in 2D. *EPL* **2013**, *104*, 21001−21006.
(45) Mattos, T. G.; Harnau, L.; Dietrich, S. Many-Body Effects for Critical Casimir Forces. *J. Chem. Phys.* **2013**, *138*, 074704−074714.
(46) Noruzifar, E.; Wagner, J.; Zandi, R. Scattering Approach for Fluctuation-Induced Interactions at Fluid Interfaces. *Phys. Rev. E* **2013**, *88*, 042314.
(47) Noruzifar, E.; Wagner, J.; Zandi, R. Three-Body Fluctuation-Induced Interaction at Fluid Interfaces: a Strong Deviation from the Pairwise Summation. *Phys. Rev. E* **2013**, *87*, 020301.
(48) Netz, R. R. Inclusions in Fluctuating Membranes: Exact Results. *J. Phys. I* **1997**, *7*, 833−852.
(49) Ravindran, M. S.; Tanner, L. B.; Wenk, M. R. Sialic Acid Linkage in Glycosphingolipids Is a Molecular Correlate for Trafficking and Delivery of Extracellular Cargo. *Traffic* **2013**, *14*, 1182−1191.

DOI: 10.1021/acsnano.6b05706
ACS Nano 2017, 11, 314−324

(50) Evans, E.; Rawicz, W. Entropy-Driven Tension and Bending Elasticity in Condensed-Fluid Membranes. *Phys. Rev. Lett.* **1990**, *64*, 2094−2097.
(51) Vaughan, J. C.; Dempsey, G. T.; Sun, E.; Zhuang, X. Phosphine-Quenching of Cyanine Dyes as a Versatile Tool for Fluorescence Microscopy. *J. Am. Chem. Soc.* **2013**, *135*, 1197−1200.

DOI: 10.1021/acsnano.6b05706
ACS Nano 2017, 11, 314−324